Free-surface deformations induced by three-dimensional turbulence

Michaël Berhanu and Eric Falcon*
Université Paris Cité, CNRS, MSC Laboratory, UMR 7057, F-75013 Paris, France

We report the experimental characterization of free-surface deformations generated by three-dimensional homogeneous and isotropic turbulence. Using Fourier transform profilometry in a jet-forced turbulent tank, we perform spatiotemporal measurements of the surface elevation field over a wide range of turbulence intensities. The standard deviation of surface deformations scales linearly with subsurface velocity fluctuations. The spectra of surface deformations highlight the coexistence of two mechanisms: transient coherent structures (e.g., upwelling) contributing to the low-frequency, large-scale spectral components, and a passive response to subsurface turbulent pressure fluctuations responsible for the power-law spectral scaling. The wavenumber and frequency spectra of surface deformations exhibit similar power-law exponents (-2.5), suggesting the advection of turbulent structures at the free surface. We develop a linear response model based on the transfer function from the free surface to turbulent pressure fluctuations, incorporating wave-turbulent damping. The model successfully predicts the main features of the turbulent surface: spatiotemporal spectrum shape, similar spectrum power-law exponents ($-7/3$), and dominance of passive response over wave generation. These findings provide new insights into free-surface turbulence in regimes where turbulent velocities remain below the surface-breaking threshold.

I. INTRODUCTION

The interaction between turbulent flows and free surfaces is fundamental to numerous geophysical and industrial processes, from ocean dynamics and atmospheric exchanges to chemical engineering applications. Understanding how subsurface turbulence deforms a free interface remains challenging due to the complex coupling between turbulent velocity and pressure fields and the surface boundary conditions imposed by gravity and surface tension. A central question is whether surface deformations result primarily from resonant generation of propagating waves or from passive response to subsurface turbulent pressure fluctuations.

Previous theoretical work has identified two main mechanisms for surface deformation generation by turbulence in air or in water. First, Phillips [1] proposed that turbulent wind pressure fluctuations could resonate with surface waves, generating propagating gravity-capillary waves when the mean flow velocity matches the wave phase velocity. This nonlinear resonance mechanism has been refined by work showing the importance of matching both velocity and length scales [2]. Second, in nonresonant conditions where this matching criterion is not satisfied, turbulence deforms mainly the free surface by the passive response to pressure fluctuations [3]. Recent developments have provided linear transfer function approaches to model this passive response [4]. Numerical investigations using direct numerical simulations (DNS) have provided insights into bubble entrainment, wave breaking dynamics, and the interplay between surface tension and turbulence [5, 6]. Studies of gas transfer rates using active grid turbulence have demonstrated that vertical turbulence intensity correlates strongly with interfacial exchange, while surface deformations were found to play a minor role [7]. Experimental studies of breaking bores provide a classification of complex air-water interfacial features [8], refining the initial Brocchini and Peregrine's classification [3]. Free-surface behaviors of shallow turbulent flows have been reviewed [9], emphasizing the need for better links between bulk flow parameters and surface patterns.

When turbulence occurs only in the liquid, and the air effect is negligible, experimental advances have improved our understanding of free-surface turbulence, although results depend on the flow configuration. Studies using grid-generated turbulence in open channel flows have observed various surface patterns, including upwellings, downdrafts, and spiral eddies [10, 11], or propagation of gravity-capillary waves without highlighting the mechanism of their generation [12]. In configuration with zero mean flow, recent experimental work using three-dimensional (3D) turbulence random-jet-stirred in close tanks has provided a detailed characterization of 3D turbulence beneath a free surface [13, 15], confirming some theoretical predictions [16–18]. In particular, a strong anisotropy develops beneath the surface with enhanced horizontal turbulent kinetic energy, decreased vertical velocity fluctuations, and amplified large-scale horizontal velocity spectra [13]. The role of upwellings and downwellings has also been documented [19], reflecting visible surface features (such as scars and dimples) [3, 20] as well as strong surface-to-bulk correlations [21]. Numerical simulations of a similar configuration showed low-frequency structures (upwellings and downwellings) dominating over waves [22]. Studies have also examined the interaction between forced surface waves and subsurface

* eric.falcon@u-paris.fr

turbulence [23–26], revealing complex advection and scattering phenomena. In particular, turbulent flows strongly damp surface waves [24]. Despite these advances, comprehensive spatiotemporal measurements of purely turbulence-generated surface deformations across a wide range of turbulence intensities remain scarce, particularly in regimes where nonresonant mechanisms may dominate. Furthermore, quantitative comparisons between experimental observations and theoretical models have been limited.

Here, we experimentally investigate free-surface deformations induced by 3D homogeneous and isotropic hydrodynamic turbulence with zero mean flow using randomly actuated jets. We observe various surface features, including scars, upwellings, and gravity-capillary waves. Using spatiotemporal measurements of the free-surface deformations across a broad parameter space, we characterize the amplitude scaling, spectral properties, and physical nature of these deformations over a wide range of turbulence levels, reaching significant surface steepness (up to 0.1). We develop a model based on the linear transfer function of the free surface responding to turbulent pressure fluctuations, incorporating realistic turbulent damping effects. Our experimental results reveal the coexistence of passive response, creating advected structures and propagating gravity-capillary waves. The passive response model captures some features of the turbulent surface, including identical power-law exponents in both spatial and temporal spectra of surface deformations. These findings complement recent advances in understanding free-surface turbulence and provide new quantitative insights into the nonresonant regime of turbulence-interface interactions.

II. EXPERIMENTAL SETUP

A. Turbulence generation

We generate three-dimensional turbulence in a square glass tank (40×40 cm^2, 66 cm deep) using an array of 64 vertical water jets arranged in an 8×8 square grid at the tank bottom (see Fig. 1). The jet orifices have an internal diameter of 1.65 cm and are spaced 5 cm apart. A variable-flow pump supplies water through electronically controlled solenoid valves. The valves open and close randomly with controlled timing, maintaining exactly 16 active jets at any instant. This forcing creates statistically stationary, spatially homogeneous turbulence in the bulk flow with almost no mean flow [13]. A detailed description and characterization of this experimental setup can be found in our recent publication [13]. The flow rate is controlled via a proportional-integral-derivative (PID) feedback system, allowing precise adjustment of turbulence intensity. We characterized the turbulence properties using particle image velocimetry (PIV) measurements of the horizontal velocity field at various depths [13]. The turbulence is homogeneous and isotropic for depths deeper than −6 cm. The root-mean-square velocity fluctuations $\sigma_{\mathcal{U}}$ (averaged over depth $z \in [-9, -7]$ cm and horizontal $x \in [-5, 5]$ cm) serve as our control parameter. It reads $\sigma_{\mathcal{U}} \equiv \sqrt{(2\sigma_u^2 + \sigma_w^2)/3}$ [14], where $\sigma_u \equiv \left\langle \sqrt{\overline{u^2(x,t)}} \right\rangle_x$, $\sigma_w \equiv \left\langle \sqrt{\overline{w^2(z,t)}} \right\rangle_z$ and ranges from $\sigma_{\mathcal{U}} = 0.65$ to 11 cm/s in this study. These velocity fluctuations are typically found 10 times stronger than the mean flow. The dissipation rate is $\epsilon \in [0.01, 71]$ cm^2/s^3 [13]. The integral length scale of the turbulence is approximately $L \approx 8$ cm, independent of forcing intensity [13]. Beneath the free surface, a redistribution of turbulent kinetic energy from vertical to horizontal fluctuations is observed [13], consistent with theoretical predictions [16, 17]. The turbulent Reynolds number $\mathrm{Re} \equiv \sigma_{\mathcal{U}} L/\nu$ ranges $\mathrm{Re} \in [523, 8801]$ and the Taylor microscale Reynolds number $\mathrm{Re}_\lambda \equiv \sigma_{\mathcal{U}}^2 \sqrt{15/(\nu\epsilon)}$ ranges $[137, 558]$ with ν the kinematic viscosity of water. The influence of the flow inertia (i.e., turbulent kinetic energy) leading to surface deformations with respect to gravity, g, preventing deformations, is quantified by the Froude number $\mathrm{Fr} \equiv \sigma_{\mathcal{U}}/\sqrt{2gL}$ in the range $[0.52, 8.8] \times 10^{-2}$. The influence of the flow inertia with respect to the surface tension is quantified by the Weber number $\mathrm{We} \equiv \sigma_{\mathcal{U}}^2 L\rho/(2\gamma)$ in the range $[0.028, 8.1]$ ($\rho = 1000$ kg/m^3 is the water density and $\gamma \simeq 60$ mN/m is the air-water surface tension). These parameters correspond to a domain where the free surface is not breaking and where weak turbulence, waves, and scars coexist on the surface [3]. Another relevant parameter is the characteristic time scale $\sqrt{g/L} \simeq 0.09$ s. The above Froude number can be thus interpreted as the ratio of this time to L/σ_U, meaning that a small Froude number corresponds to a slow turbulent flow compared to the relaxation time of a perturbation of size L under gravity.

B. Surface measurement technique

We measure the free-surface elevation field $\eta(x, y, t)$ using Fourier transform profilometry (FTP) [27–29]. This nonintrusive optical technique projects a sinusoidal fringe pattern onto the free surface using a full-HD video projector (Epson EH-TW3200) positioned above the tank. Surface deformations distort the fringe pattern, which is recorded by a high-speed camera (Phantom V10). Fourier analysis of each image extracts the phase field, from which the surface elevation is reconstructed using a calibrated phase-to-height relationship [28]. The measurement domain covers a surface $\mathcal{S} = 20.3 \times 16.4$ cm^2 at the top tank center with a spatial resolution of about 4 mm (roughly 3 times the fringe

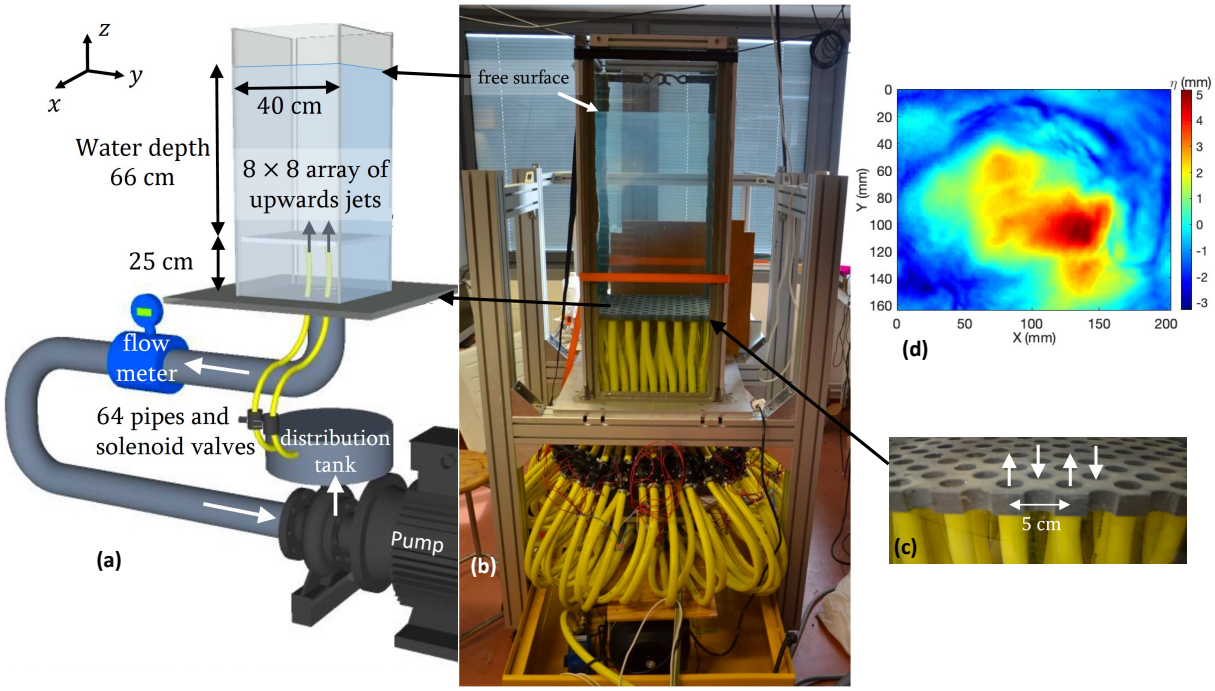


FIG. 1. (a) Schematic diagram of the experimental setup used to produce bulk turbulence, with almost no mean flow, within a square glass tank of side 40 cm. Water depth: 66 cm. (b) Side view of the experimental setup where 64 upward jets, arranged in an 8×8 square grid with a 5-cm spacing, are placed in the gray slab, 25 cm above the tank bottom. (c) Close-up view of the jet orifices (upward arrows) inside the slab and the suction holes (downward arrows) located at the center of each square formed by the inlet jets. (d) Typical water free-surface deformations $\eta(x, y)$ measured in a 20.3×16.4 cm^2 zone (at the tank top center), using Fourier transform profilometry (FTP), for moderate subsurface turbulence ($\sigma_{\mathcal{U}} = 5.1$ cm/s).

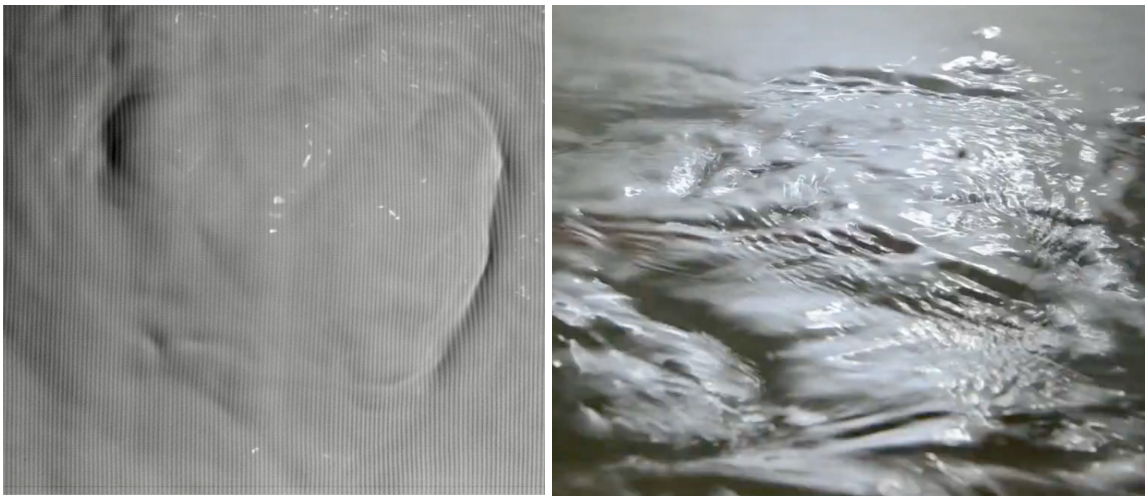


FIG. 2. Typical surface deformations: (Left) for gentle turbulence showing surface scarification and upwellings as imprints of subsurface turbulence (top view with fringes of the FTP method - 20.3×16.4 cm^2), and (Right) for moderate turbulence showing scars and waves (typical size 1 cm) (oblique view).

distance). We acquire data at 300 frames per second for $\mathcal{T} = 52$ s, providing excellent temporal resolution for analyzing both advected structures and propagating waves. To obtain good optical contrast, we seed the water surface with a controlled amount of micrometric titanium dioxide (TiO_2) particles [30]. Previous studies have confirmed that TiO_2 particles do not alter the water surface tension and viscosity [31], ensuring that the measurements remain unaffected by the seeding particles.

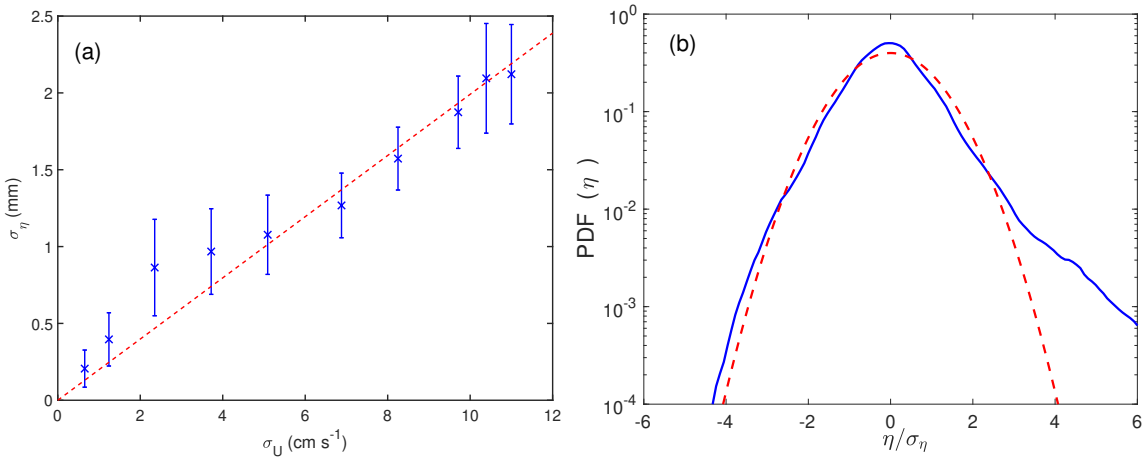


FIG. 3. (a) Standard deviation of surface deformations σ_η versus subsurface turbulent velocity fluctuations $\sigma_\mathcal{U}$. σ_η scales linearly with turbulence intensity. The dashed red line has a slope of 0.02 s. Errobars correspond to the spatial variation of the standard deviation over $\mathcal{S}$. (b) Probability density function (PDF) of the normalized surface deformations, η/σ_η, for $\sigma_\mathcal{U} = 10.4$ cm/s. Dashed red line: Normal distribution.

III. EXPERIMENTAL RESULTS

A. Free-surface deformation amplitude

Figure 2 shows typical surface deformations in response to subsurface turbulence. For gentle turbulence (Fig. 2a), surface scarifications are visible as imprints of subsurface turbulence and vortices, whereas for moderate turbulence (Fig. 2b), scars and waves are observed simultaneously (see a movie in Ref. [32]). An example of the free-surface deformation amplitude, $\eta(x, y)$, obtained by FTP is shown in Fig. 1d and is of the order of a few mm for moderate turbulence. The standard deviation of surface elevation $\sigma_\eta \equiv \sqrt{\int_\mathcal{S} [\langle \eta^2(x, y, t)\rangle_t - \langle \eta(x, y, t)\rangle_t^2]\, \mathrm{d}x\, \mathrm{d}y}$ is displayed in Fig. 3a as a function of subsurface turbulent velocity fluctuations $\sigma_\mathcal{U}$. The relationship is roughly linear across the entire range

$$\sigma_\eta \approx K \sigma_\mathcal{U} \tag{1}$$

with $K = 0.02$ s and a maximum value of $\sigma_\eta \approx 2$ mm. This linear scaling suggests that the mechanism generating surface deformations remains consistent across all turbulence levels investigated. We observe that the prefactor K is of the same order of magnitude as the timescale obtained from dimensional analysis $\sqrt{L/g} \approx 0.09$ s, which has been introduced in Sect. II A. We define a mean steepness $\kappa \equiv k_{\max}\sigma_\eta$, where $k_{\max} = 46$ m^{-1} is the wavenumber of maximum energy in the spatial spectrum of deformation amplitudes (discussed below in Sect. III C). The steepness reaches $\kappa \approx 0.1$ at the highest forcing, representing significant surface deformations. The absence of any threshold behavior in the σ_η vs. $\sigma_\mathcal{U}$ relationship indicates that surface deformation generation does not require a critical turbulence intensity. Note that when the turbulence intensity is further increased, transient humps appear on the surface beneath jets, a case which will not be studied here. Figure 3b shows the probability density function (PDF) of the surface deformations $\eta(x, y, t)$, averaged over space and time, normalized by its rms value, σ_η, for strong turbulence. The PDF is skewed with more probable positive deformations than negative ones, as a signature of upwelling events.

B. Spatiotemporal spectrum of surface deformations

To elucidate the physical nature of surface deformations, we compute the spatiotemporal power spectrum $S_\eta(k, \omega)$ of the free-surface deformations. Such a spectrum reveals whether the surface exhibits propagating waves (concentrated along dispersion relation curves) or non-propagating advected structures (concentrated near $f \simeq 0$). Due to the isotropy of the deformations, the spatiotemporal power spectrum of the free-surface deformations, $S_\eta(k, \omega)$, is obtained as $S_\eta(k, \omega) = \int_k S_\eta(k_x, k_y, \omega) dk_x dk_y$ with $k \equiv \sqrt{k_x^2 + k_y^2}$ and $S_\eta(k_x, k_y, \omega) \equiv |\int \hat{\eta}(k_x, k_y, t) e^{i\omega t} dt|^2/(2\pi\mathcal{ST})$.

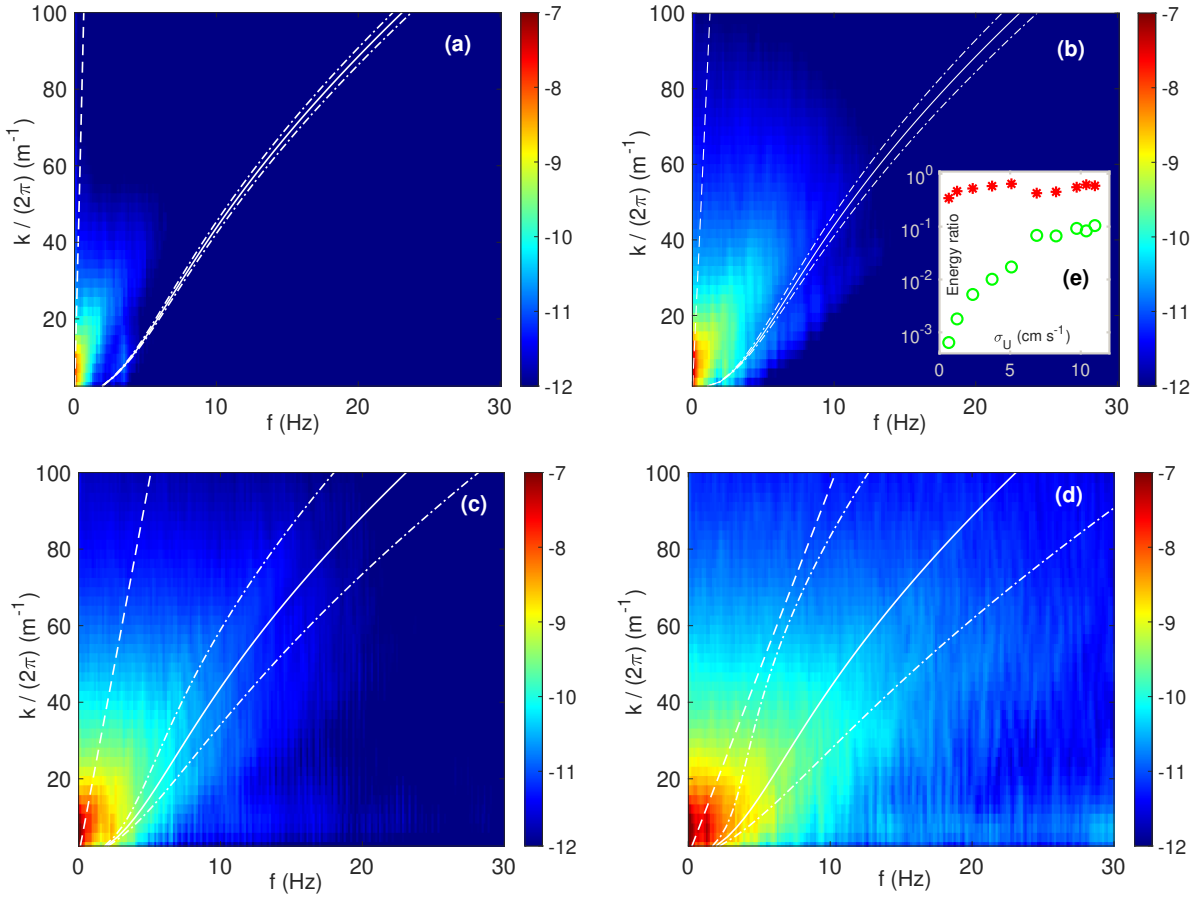


FIG. 4. Spatiotemporal power spectra $S_\eta(k,\omega)$ of free-surface deformations for different subsurface turbulence: weak (a) $\sigma_{\mathcal{U}} = 0.65$ cm/s and (b) $\sigma_{\mathcal{U}} = 1.24$ cm/s, (c) moderate turbulence $\sigma_{\mathcal{U}} = 5.1$ cm/s, and (d) strong turbulence $\sigma_{\mathcal{U}} = 10.4$ cm/s. Logarithmic-scale colorbars in m^3 s. White solid curves: dispersion relation of Eq. (2) with $\sigma_{\mathcal{U}} = 0$, i.e., without large-scale random flow advection. White dashed lines: $\omega = k\sigma_{\mathcal{U}}$ (pure advected structures). White dash-dotted curves: Doppler-shifted dispersion relation of Eq. (2) (advected gravity-capillary waves) with corresponding values of $\sigma_{\mathcal{U}}$. (e) Energy contained within the advection cone ($\omega \leq k\,\sigma_{\mathcal{U}}$) (red stars) or within the Doppler-broadened dispersion relation (i.e., between the two white dash-dotted lines) (green circles) as a function of $\sigma_{\mathcal{U}}$ (semilog-y). This normalized energy is computed by dividing the spectrum integral over the chosen region by the integral over the full domain.

$\hat{\eta}(k_x, k_y, t) \equiv \int \eta(x,y) e^{-i(k_x x + k_y y)} dxdy/(2\pi)$ is the 2D spatial Fourier transform of the surface deformation amplitude $\eta(x,y)$ of each image recorded at time t.

Figure 4 shows the spatiotemporal spectra, $S_\eta(k,\omega)$, for different turbulence levels $\sigma_{\mathcal{U}}$. For gentle turbulence (Fig. 4a-b), we observe an energy concentration near $f \simeq 0$ in the spectra, whereas for moderate (Fig. 4c) and strong (Fig. 4d) turbulence, energy broadening occurs in both frequency and wavenumber. To interpret these spectra, we must account for the Doppler shift due to random large-scale advection beneath the surface (although almost no bulk mean flow is present [13]). For gravity-capillary waves propagating on a medium in the presence of random large-scale advection of strength $\sigma_{\mathcal{U}}$, the dispersion relation reads

$$\omega = \sqrt{gk + \frac{\gamma k^3}{\rho}} \pm k\sigma_{\mathcal{U}} \tag{2}$$

where g is gravitational acceleration, γ is surface tension, and ρ is water density. The white dash-dotted curves in Fig. 4 correspond to Eq. (2) and the white solid ones to Eq. (2) with $\sigma_{\mathcal{U}} = 0$, i.e., without random large-scale advection. For gentle turbulence (Fig. 4a-b), no gravity-capillary wave is generated and a significant portion of energy concentrates along the line $\omega = k\sigma_{\mathcal{U}}$ (white dotted lines in Fig. 4), corresponding to random large-scale advection. This energy dominates over that of propagating waves, contrasting with the results of Savelsberg and van de Water (turbulent current with a strong mean flow in an open channel) [12] but consistent with numerical simulations by

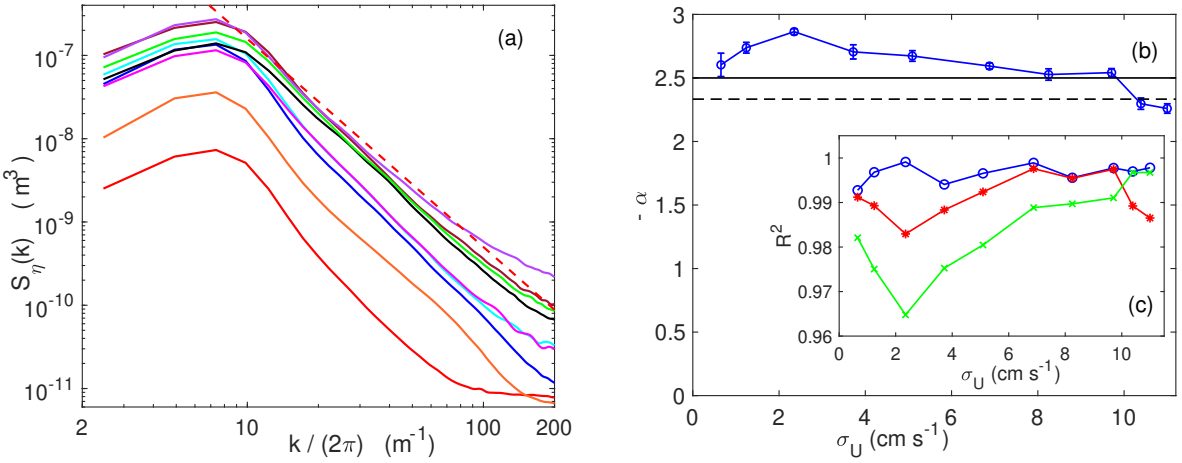


FIG. 5. **(a)** Spatial power spectra $S_\eta(k)$ for different turbulence intensities $\sigma_\mathcal{U} = 0.65$, 1.2, 2.4, 3.7, 5.1, 6.9, 8.3, and 10.4 cm/s (from bottom to top). The red dashed line shows the power law $k^{-2.5}$ in the intermediate range. All spectra exhibit similar shapes with consistent power-law exponents. The integral scale of the subsurface turbulence is $1/L \approx 12.5$ m^{-1}. **(b)**: (+) experimental spatial-spectral exponent α obtained by fitting a linear polynomial to $\log[S_\eta(k)]$ vs $\log(k)$ using the least-squares method. Error bars correspond to the 95% confidence interval. Black and dashed lines correspond to -2.5 and $-7/3$ values, respectively. By averaging over the different runs (and removing the first run), the mean spatial exponent is $\alpha = -2.58 \pm 0.20$ (uncertainty is the standard deviation). **(c)** Goodness-of-fit coefficients R^2: (∘) for the fit presented in (b), (∗) for the fit by the power law $A\,k^{-2.5}$, and (×) by $A'\,k^{-7/3}$. Values of R^2 above 0.9 show that both fits are acceptable, although the first one is better.

Guo and Shen [22] for similar configurations (no mean flow and finite domain).

It should be noted that if the spectrum is computed along a single horizontal direction (i.e., not integrated over all directions), the gravity-capillary surface-wave dispersion relation can be shifted by a mean flow (not shown). This occurs for weak forcing, where the fully developed turbulence regime is not achieved, and for measurement durations shorter than those in [13]. However, this mean-flow effect is not dominant compared to that of surface fluctuations, as the shifted dispersion-relation branch is no longer visible when the spectrum is integrated over all directions.

For strong enough turbulence (Fig. 4c-d), part of the spectral energy distribution is located around the dispersion relation curve, indicating the presence of gravity-capillary waves generated by the turbulent flow. However, the energy spreads more broadly due to Doppler effects: the velocity fluctuations of turbulent eddies advecting waves create a frequency broadening for each wavenumber. This spectral broadening is thus different from the classical nonlinear broadening of weak wave turbulence occurring only near the dispersion relation [29, 33]. Here, the Doppler broadening from turbulent velocity fluctuations increasingly spreads spectral energy both spatially and temporally. This makes it difficult to distinguish between energy from propagating waves (which would concentrate along dispersion curves without advection) and low-frequency advected structures (which would concentrate near $f \simeq 0$ without advection). To quantify the magnitude of each contribution, we also compute the energy ratio by dividing the spectrum integral over a specified domain by the integral over the full range. As shown in Fig. 4e, the spectrum energy contained within the advection cone for $\omega \leq k\sigma_\mathcal{U}$ (red stars) is much larger than the one within the Doppler-broadened dispersion relation [Eq. (2)], although the latter significantly increases with $\sigma_\mathcal{U}$.

Consistently, using spatial and temporal spectral analyses, the evidence points to the continued dominance of advected low-frequency structures across all turbulence levels.

C. Spatial spectrum of surface deformations

The spatial power spectrum, $S_\eta(k) \equiv \int S_\eta(k,\omega)d\omega$, is obtained by integrating the spatiotemporal spectrum over all frequencies. Figure 5 shows such spectra for all turbulence intensities $\sigma_\mathcal{U}$ investigated, and reveals the spreading of surface deformation energy across spatial scales. All spectra exhibit remarkably similar shapes with a maximum at $k_{\max}/(2\pi) \approx 7.4$ m^{-1} (i.e., $k_{\max} \approx 46$ m^{-1} or wavelength $\lambda_{\max} \approx 13.5$ cm), slightly larger than the integral length scale $L \approx 8$ cm, as found for the velocity spectrum below the surface in the homogeneous region [13]. For intermediate scales $(k/(2\pi) \in [10, 100]$ m^{-1} or $\lambda \in [1, 10]$ cm, corresponding to the gravity-capillary wave regime), the spectra

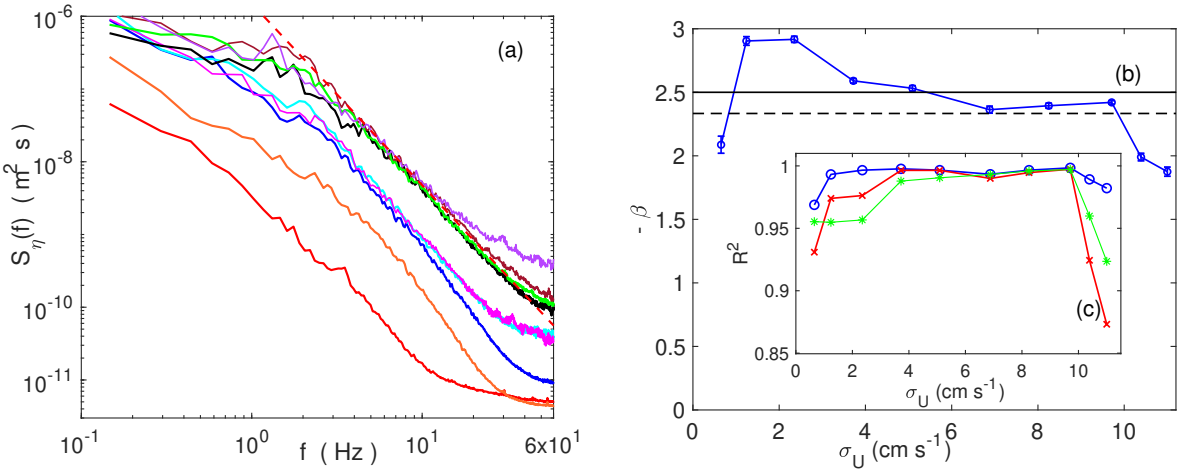


FIG. 6. **(a)** Frequency power spectra $S_\eta(f)$ for different turbulence intensities $\sigma_\mathcal{U}$ = 0.65, 1.2, 2.4, 3.7, 5.1, 6.9, 8.3, and 10.4 cm/s (from bottom to top). The red dashed line shows the power law $f^{-2.5}$ in the inertial range. The similarity with spatial spectral exponents suggests advection-dominated dynamics. **(b)**: (+) Experimental temporal-spectral exponent β obtained by fitting a linear polynomial $\log[S_\eta(\omega)]$ vs $\log(\omega)$ using the least-squares method. Error bars correspond to the 95% confidence interval. Black and dashed lines correspond to -2.5 and $-7/3$ values, respectively. By averaging over the different runs (and removing the first run), the mean frequency exponent is $\beta = -2.44 \pm 0.35$ (uncertainty is the standard deviation). **(c)**: Goodness-of-fit coefficients R^2: (∘) for the fit presented in (b), (×) for the fit by the power law $B\,f^{-2.5}$, and (∗) by $B'\,f^{-7/3}$. Values of R^2 above 0.9 show that both fits are acceptable, although the first is better.

follow a power law:

$$S_\eta(k) \propto k^\alpha \tag{3}$$

over one decade in k with exponent $\alpha = -2.58 \pm 0.2$ consistent across all turbulence levels, as shown in Fig. 5b. Given the uncertainties, this exponent can be approximated to $\alpha \approx 2.5$. This power-law exponent differs markedly from that ($\alpha \approx -6$) found when surface dynamics is dominated by waves in the presence of subsurface turbulence in a channel with a mean flow [12]. Instead, our value is consistent with studies for quasi-two-dimensional turbulent flows where no waves were observed (α between -2 and -3.5) [34]. The spatial exponent $\alpha \approx -2.5$ is close to theoretical predictions for several scenarios. For gravity waves, weak turbulence theory predicts $\alpha = -5/2 = -2.5$ [29, 35, 36], and at stronger forcing, a saturated spectrum (flux-independent solution) predicted by Phillips with $\alpha = -3$ [38], both compatible with field observations in ocean [39]; whereas for capillary waves, weak turbulence predicts an exponent $-15/4 = -3.75$ [29, 36, 40]. However, our spatiotemporal spectra at gentle turbulence clearly showed that low-frequency advected structures dominate over propagating waves. A plausible alternative interpretation is that surface deformations passively respond to subsurface turbulent pressure fluctuations. From hydrostatic balance, $\eta \approx p/(\rho g)$, where p represents pressure fluctuations. The spatial structure of turbulence-induced surface deformations should therefore mirror the structure of the subsurface pressure field. Models and experiments show that the spatial spectrum of a turbulent pressure field p scales as $S_p(k) \propto k^{-7/3}$ at sufficiently high Reynolds numbers [41–43], close to our observed $k^{-2.5}$ scaling. Recent numerical simulations of the air-water interface, with turbulence in the water phase, show that the pressure spectrum acting on the free surface follows the power law $S_p(k) \propto k^{-7/3}$ resulting from homogeneous isotropic turbulence despite possible flow anisotropy in the vicinity of the interface [37]. While the spectra are better fit by a power law with an exponent $\alpha = -2.5$, our data are also satisfactorily fit with an exponent $\alpha = -7/3$ (see Fig. 5c). The consistent power-law exponent and spectral shape across all turbulence intensities suggest that the same deformation mechanism operates throughout our parameter range, supporting the passive response hypothesis.

D. Frequency spectrum of surface deformations

Frequency power spectra, $S_\eta(\omega) \equiv \int S_\eta(k,\omega)dk$, obtained by integrating spatiotemporal spectra over all wavenumbers, characterize the frequency content of surface deformations. Figure 6 shows these spectra for all turbulence levels. For intermediate turbulence intensities (excluding the weakest), the inertial range ($f \in [2, 30]$ Hz) exhibits a power

law:

$$S_\eta(f) \propto f^\beta \tag{4}$$

with $\beta = -2.44 \pm 0.35$ across these cases, as shown in Fig. 6(b). Similarly, given the uncertainty, this exponent can be approximated as $\beta \approx -2.5$. For propagating waves, spatial and temporal spectra are related through the dispersion relation $\omega \sim k^\zeta$. Specifically, if $S_\eta(k) \propto k^\alpha$ and $S_\eta(f) \propto f^\beta$, dimensional analysis then leads to $\beta = (\alpha+1)/\zeta - 1$ [36]. Thus, for gravity waves ($\omega = \sqrt{gk}$, i.e., $\zeta = 1/2$) and for $\alpha = -2.5$, one should have $\beta = -4$, and weak gravity-wave turbulence theory indeed predicts $\beta = -4$ [35, 36] as well as Phillips' theory for wind-generated resonant waves [44], whereas Phillips' saturated spectrum predicts $\beta = -5$ [38]. For capillary waves ($\omega = \sqrt{\gamma k^3/\rho}$, i.e., $\zeta = 3/2$), $\alpha = -2.5$ should lead to $\beta \approx -2$ whereas weak capillary-wave turbulence predicts $\beta = -17/6 \approx -2.8$ and $\alpha = -15/4 = -3.75$ [36, 40]. However, here, we observe $\beta \approx \alpha \approx -2.5 \pm 0.3$, indicating that temporal and spatial power-law exponents are nearly equal rather than related by the dispersion relationship. This similarity can be explained if low-frequency structures are advected by the flow. For such advected structures with $\omega \approx kv$ (i.e., $\zeta = 1$) where v is a characteristic velocity of the subsurface flow, we have $d\omega/dk \approx v$, leading to $\beta \approx \alpha$. We verified that subsurface turbulent structures satisfy Tennekes' frozen turbulence hypothesis in our flow, consistent with advection dominating over intrinsic dynamics for turbulent eddies [13]. The concordance between experimental spatial and temporal power-law exponents ($\beta \approx \alpha$) therefore supports the hypothesis that low-frequency advected structures dominate surface deformations, rather than propagating waves, across most turbulence levels studied. In Fig. 6(c), we show that the temporal spectra are satisfactorily fit by the $f^{-2.5}$ power law and slightly less so by $f^{-7/3}$. This last relation is also expected in the case of advection by the turbulence of the spatial spectrum associated with pressure fluctuations.

IV. MODEL OF PASSIVE RESPONSE TO TURBULENT PRESSURE FLUCTUATIONS

To further investigate the passive response mechanism and describe our experimental observations, we develop a model for the linear response of a liquid surface subjected to an arbitrary normal N and tangential $\mathbf{T}$ stress fields in a statistically steady and homogeneous regime, following the approach of Perrard et al. [4]. After linearization of the Navier-Stokes equations with such free-surface boundary conditions, the spatiotemporal Fourier transform of the surface elevation reads [4]

$$\hat{\eta}(\mathbf{k}, \omega) = \frac{k\hat{N} + i\mathbf{k} \cdot \hat{\mathbf{T}}}{\rho(\omega^2 - gk - \gamma k^3/\rho + i2\omega\delta)} \tag{5}$$

where the denominator represents the transfer function of the free surface, and $\hat{N}$ and $\hat{\mathbf{T}}$ are the Fourier components of the applied stresses. The real part of the denominator vanishes when the forcing satisfies the surface wave dispersion relation $\omega(k) = \sqrt{gk - \gamma k^3/\rho}$, leading to resonance that is saturated by the dissipative term [imaginary part of the denominator involving a wave damping rate $\delta(\omega)$].

We evaluate the free-surface response to turbulent pressure fluctuations in the liquid phase below the free surface, assuming negligible stresses in the gas phase. For homogeneous isotropic turbulence, the 1D pressure spatial power spectrum is predicted to follow [41]

$$S_P^{1\mathrm{D}}(k) = C\rho^2\epsilon^{4/3}k^{-7/3} \tag{6}$$

where ϵ is the turbulent energy dissipation rate, and $C = 3.59$ is a constant. This power law is verified experimentally [42, 43], and the constant is close to 8 ± 0.5 numerically [45]. Although turbulence becomes anisotropic near the free surface [13], pressure P is a nonlocal field resulting from integration of velocity gradient source terms with $1/r$ decay (Poisson equation inversion). We assume thus that the pressure spectrum in the water phase at the free surface follows Eq. (6). This hypothesis is supported by recent numerical simulations [37] showing that the pressure spectrum at an air-water free surface follows a power law in $k^{-7/3}$. As normal stress forcing N strongly dominates tangential stress $\mathbf{T}$ in turbulence [4], especially in the absence of mean shearing flow, we assume $N = P$ and $T = 0$. For the pressure spectrum $S_P(k, \omega)$, we use the random sweeping model assuming that the small-scale fluctuations in a turbulent flow are randomly swept by the large-scale fluctuations [47]. The spatiotemporal spectrum consists of a spatial spectrum multiplied by a Gaussian frequency distribution, read (when averaged over horizontal directions) [47]

$$S_P(k, \omega) = \frac{S_P^{1\mathrm{D}}(k)}{\sqrt{2\pi k^2 V^2}} \exp\left[-\frac{(\omega - kU)^2}{2k^2V^2}\right] \tag{7}$$

with U the mean flow velocity, $V = \sigma_{\mathcal{U}}$ the sweeping velocity, and $\sigma_{\mathcal{U}}$ the rms amplitude of turbulent velocity fluctuations (see Sect. II A). This model has interesting properties. The mean velocity leads to a Doppler shift in frequencies, whereas the sweeping velocity broadens the spectrum in the frequency domain. From integration of Eq. (7), the frequency spectrum exhibits the same spectral power-law exponent as the spatial spectrum, independent of the mean and sweeping velocities. Taking the square modulus of Eq. (5), the power spectrum of surface deformations $S_\eta(k,\omega)$, as the response to $S_P(k,\omega)$ of Eq. (7), is given by

$$S_\eta(k,\omega) = \frac{k^2 S_P(k,\omega)}{\rho^2|\omega^2 - gk - \gamma k^3/\rho + i2\omega\delta|^2} \tag{8}$$

A crucial aspect is that turbulence strongly attenuates the waves it might create. We use the damping rate due to turbulence, $\delta_u = C_\delta\, \sigma_{\mathcal{U}} k (Lk)^{-1/3}$, with L the integral scale [24, 48]. δ_u expresses the wave energy transfer to the bulk flow by estimating the turbulent mixing rate over a depth of $1/k$, which is also proportional to $\sigma_{\mathcal{U}}$. C_δ is a dimensionless prefactor of order one [48]. The value $C_\delta = 1$ is used henceforth, and the effect of varying C_δ is discussed in Appendix A. Such turbulent damping of waves generally dominates viscous damping $\delta_{\nu_0} = 2\nu k^2$ (for the uncontaminated surface case), and even for fully contaminated surfaces where $\delta_\nu = k\sqrt{\nu\omega}/(2\sqrt{2})$ [49, 50]. We take $\delta = \delta_u + \delta_\nu$, representing a typical inverse lifetime of surface fluctuations.

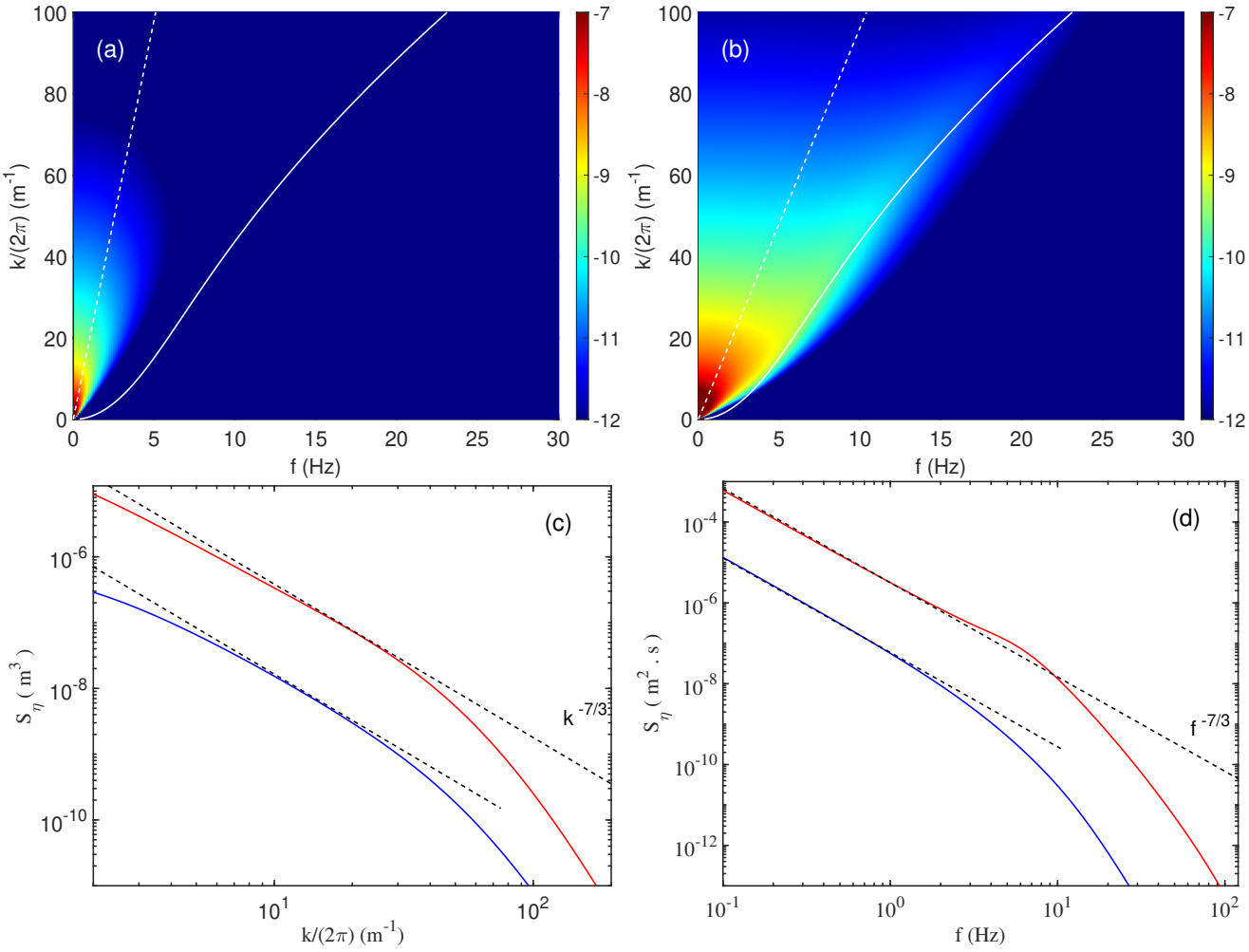


FIG. 7. Model predictions: Spatiotemporal spectra of surface deformations $S_\eta(k,\omega)$ for (a) weak subsurface turbulence ($\sigma_{\mathcal{U}} = 5.1$ cm/s) and (b) strong turbulence ($\sigma_{\mathcal{U}} = 10.4$ cm/s). Logarithmic-scale colorbars in m^3 s. $C_\delta = 1$. White dotted lines: $\omega = \sigma_{\mathcal{U}} k$. White curves show the gravity-capillary dispersion relation of Eq. (2) with $\sigma_{\mathcal{U}} = 0$. Model predictions: Spatial (c) and temporal (d) power spectra of surface deformation for (blue) weak subsurface turbulence ($\sigma_{\mathcal{U}} = 5.1$ cm/s) and (red) strong turbulence ($\sigma_{\mathcal{U}} = 10.4$ cm/s). The dashed lines are $k^{-7/3}$ (c) and $f^{-7/3}$ (d) power laws.

Using our experimental parameters ($L = 8$ cm, $\epsilon = A\sigma_{\mathcal{U}}^3/L$, A=0.42, no mean flow $U = 0$) [13] and Eq. (6) with $C = 3.59$, we compute predictions of Eqs. (7) and (8) for two turbulent velocity fluctuations $\sigma_{\mathcal{U}}$. First, we check

that the pressure spectrum is consistent with previous direct numerical simulations [51]. Figure 7a then shows the surface deformation spectrum for weak turbulence ($\sigma_{\mathcal{U}} = 5$ cm/s). The energy is mainly concentrated in the region $\omega \leq \sigma_{\mathcal{U}} k$, and energy is absent on the dispersion relation (white line). These features closely resemble the pressure fluctuation spectrum, indicating a passive response (not shown). For stronger turbulence ($\sigma_{\mathcal{U}} = 10$ cm/s), the surface spectrum extends over a broader (ω,k) region (see Fig. 7b), qualitatively resembling our experimental spatiotemporal spectra in Fig. 4d. Surface waves are excited for this level of damping, δ_u. However, the dispersion relation appears more clearly visible in the model than in the experiment. Our model does not address how the dispersion relation is modified in the laboratory frame by turbulent advection (Doppler broadening) (Eq. 2). In the experiments, we expect that the dispersion relations are significantly broadened. In Appendix A, we address cases of weaker magnitude of the turbulent dissipation δ_u. Specifically, if we neglect δ_u and retain only viscous dissipation, δ_ν (contaminated surface case), more energy appears along the wave dispersion relation at strong $\sigma_{\mathcal{U}}$.

By integrating the spatiotemporal spectrum $S_\eta(k,\omega)$ of Eq. (8) in ω or in k, the predicted spectra in Fig. 7c-d show power laws $S_\eta(k) \propto k^{-7/3}$ and $S_\eta(f) \propto f^{-7/3}$ in the gravity-capillary wave range in satisfying agreement with experimental spectra of Figs. 5 and 6, respectively. Finally, the predicted rms surface fluctuations are inferred from $\sigma_\eta \equiv \sqrt{\int S(k)dk}$ leading to $\sigma_\eta \approx 3.0$ mm (resp. 0.44 mm) for $\sigma_{\mathcal{U}} = 10.4$ cm/s (resp. 5.1 cm/s) in rough agreement (given the simplifying assumptions) with the measured values 2.1 mm (resp. 1.1 mm) in Fig. 3a.

Our model thus successfully captures several key experimental observations. First, the spatiotemporal spectra show energy concentration at low frequencies in the region $\omega \leq \sigma_{\mathcal{U}} k$ rather than along the dispersion relation, consistent with advection-dominated dynamics. Second, spatial and temporal power-law exponents are similar, close to our experimental observation that $\alpha \approx \beta$ rather than the wave relation $\beta = (\alpha+1)/\zeta - 1$. Third, the predicted exponent $-7/3 \approx -2.33$ is close to our experimental value -2.5 ± 0.3, which is compatible with the passive response to turbulent pressure fluctuations. Moreover, the model predicts that turbulent damping δ_u prevents energy concentration along the dispersion relation, explaining why wave signatures remain weak in our experiments. The passive response mechanism thus creates randomly advected structures that carry the signature of subsurface pressure fluctuations. However, a significant difference between the experiments and this model is that the model predicts $\sigma_\eta \propto \sigma_{\mathcal{U}}^2$, in contrast with the linear dependence observed experimentally. Indeed, contributions to the free-surface fluctuations in the experiment may arise from other phenomena, such as large-scale coherent flow structures like upwelling or downwelling [22], which are not accounted for in our model. Minor quantitative discrepancies also appear as small differences in spectral slopes, and energy is more broadly distributed in the experiment near the dispersion relation. They likely arise from simplified assumptions in the model (homogeneous isotropic pressure spectrum near the anisotropic surface, and empirical turbulent damping formula) and from experimental precision to distinguish between $-7/3$ and -2.5 ± 0.3 exponents on a single decade scale. However, the model validates our interpretation of surface deformations as resulting partially from passive responses to turbulent pressure fields.

V. DISCUSSION

Our experimental investigation reveals that passive response to subsurface pressure fluctuations contributes significantly to surface deformations. The experimental spectra in Fig. 4 display low amplitude close to the surface wave dispersion relation, even when accounting for broadening due to turbulent fluctuations, revealing a small contribution of coherent surface waves. The passive response mechanism creates advected structures carrying the signature of turbulent pressure fields, with a spectral exponent (-2.5) for the surface deformation spectrum matching the model prediction ($-7/3$). The coexistence of passive response and weak propagating waves distinguishes our results from two limiting cases in the literature. Savelsberg and van de Water [12] observed wave-dominated surfaces in grid-stirred turbulence with a strong mean flow and a lower turbulence intensity. A clear wave signature, with a much steeper k-spectral slope (-6), is observed, without highlighting the wave creation mechanism. Conversely, Guo and Shen's simulations [22] of jet-forced turbulence without mean flow showed structure-dominated surfaces similar to ours, supporting the importance of configuration geometry in determining the dominant mechanism. The turbulent damping rate $\delta_u = C_\delta \, \sigma_{\mathcal{U}} k (Lk)^{-1/3}$ identified by Ölmez and Milgram [48] and by Gutiérrez and Aumaître [24] should play an important role in our system. Our model demonstrates that including δ_u is essential to reproduce the weak wave activity arising from the passive response to turbulent pressure fluctuations. Without turbulent damping, the model predicts much stronger wave signatures along the dispersion relation. However, our model does not describe the linear scaling $\sigma_\eta \propto \sigma_{\mathcal{U}}$ found experimentally across our range of turbulence intensities, possibly due to the large-scale coherent flow structures (such as upwelling and downwelling) characteristic of free-surface turbulence [22]. This observed linear scaling contrasts with free-surface breaking regimes where nonlinear effects become important at higher Froude numbers [6]. Our moderate Froude numbers maintain the free surface in a quasilinear response regime, validating the linear transfer function approach. Recent work on jet-forced turbulence focused on subsurface turbulence

structure rather than surface deformations, but their observation of strong upwelling/downwelling events is consistent with our interpretation [15, 19]. A linear response to a transient vertical current U_z can be described by the linear kinematics boundary condition $\partial\eta/\partial t \approx U_z$. Assuming U_z scales as $\sigma_{\mathcal{U}}$, this condition may explain the linear scaling between σ_η and $\sigma_{\mathcal{U}}$. We note, indeed, in Fig. 3a that the coefficient K of Eq. (1), with dimensions of time, is of order $\sqrt{L/g}$. $\sigma_{\mathcal{U}}$ corresponds indeed to the turbulent fluctuations at the integral scale L. This linear response to transient turbulent currents may represent the primary mechanism populating low-frequency, large-scale components of the spectra, whereas the response to pressure fluctuations is likely responsible for the observed power-law behavior. A more elaborate model combining kinetic and dynamic boundary conditions would enable a more complete description of turbulent free-surface dynamics. The coupling between large-scale coherent transient currents and turbulent fluctuations drives the passive response of the free surface. Joint measurements of surface deformations and subsurface velocity fields would enable a direct quantification of this coupling.

VI. CONCLUSION

We have reported the characterization of spatiotemporal deformations of a free surface forced by 3D homogeneous and isotropic turbulence with zero mean flow. Over a wide range of turbulence intensities, we found that the surface deformation amplitude scales linearly with subsurface velocity fluctuations ($\sigma_\eta \propto \sigma_{\mathcal{U}}$), up to a significant steepness (≈ 0.1), without exhibiting threshold behavior across the entire range. Surface deformations are strongly advected by subsurface flows. Their spatiotemporal spectra reveal the coexistence of two phenomena. First, large-scale coherent structures (upwelling) provide low-frequency surface deformation. Second, the passive response to subsurface turbulent pressure fluctuations produces, at the free surface, the footprint of the pressure spectrum filtered by the linear transfer function of the free surface. Spatial and temporal spectra of surface deformations exhibit similar wavenumber- and frequency-power-law exponents (-2.5), consistent with advection-dominated dynamics rather than free wave propagation. These spectral characteristics remain remarkably consistent across our range of turbulence levels. We also developed a linear response model based on the transfer function of the free surface to turbulent pressure fluctuations below, involving turbulent wave damping that prevents wave amplification. The model successfully predicts the main features of the free-surface dynamics: (i) spatiotemporal spectrum shape with energy concentrated at low frequencies in the region $\omega \leq \sigma_{\mathcal{U}} k$, (ii) power-law exponents $k^{-7/3}$ and $\omega^{-7/3}$ matching turbulent pressure spectra, and (iii) dominance of passive response over free wave generation. The $-7/3$ spectral-exponent prediction is compatible with experimental observations (-2.5), confirming that surface deformations primarily reflect the structure of the subsurface turbulent pressure field. In configurations lacking conditions for Phillips resonance, i.e., specifically when turbulent velocities remain below wave phase velocities ($\sigma_{\mathcal{U}} < c_w^{\min}$ the minimal phase velocity of gravity-capillary waves) and interfacial shear is weak (e.g., no mean flow), surface deformations are dominated by passive response to the turbulent pressure fluctuations beneath the free surface. The turbulent damping rate prevents significant wave generation even as forcing increases. This regime, reported here, thus differs from wave-dominated surfaces observed in grid-stirred turbulence with a strong mean flow (while remaining far from the resonance conditions for wave amplification) [12], highlighting the critical importance of flow configuration. These results complement recent advances in free-surface turbulence [6, 7, 13, 15, 19–21] and provide quantitative validation of the passive response mechanism in the nonresonant regime. This is particularly relevant to many environmental and industrial flows where wave generation conditions are not met, including regions of the ocean away from strong wind forcing, industrial mixing tanks, and flows in confined geometries. Future work could explore different forcing configurations satisfying resonance conditions to map the transition between structure- and wave-dominated regimes. A new forcing method of turbulence at small scale, using magnetic stirrers randomly driven in space and time, could also be tested in this context [52–54]. Other work could also examine the wave generation mechanism (possibly by upwellings or transient humps), and finally extend measurements to higher turbulence approaching boiling and bubble formation regimes, requiring adapted optical techniques.

ACKNOWLEDGMENTS

We thank T. Jamin for insightful discussions and early contributions to this work. We thank A. Lantheaume, Y. Le Goas, and A. Di Palma for technical support. This work was supported by the French National Research Agency (ANR TURBULON project No. ANR-12-BS04-0005 and ANR DYSTURB project No. ANR-17-CE30-0004), the DGA (Direction Générale de l'Armement, France, No. 2015600018), and the CNRS. E. F. thanks the support of the Simons Foundation Project No. MPS-WT-00651463 (U.S.), ANR Lascaturb Project No. ANR-23-CE30-0043-02, and ANR Provebact Project No. ANR-24-CE09-1394-02.

Appendix A: Effect of wave dissipation on the model of passive response to turbulent pressure fluctuations

Figure 8 shows the spatiotemporal spectra of surface deformations $S_\eta(k,\omega)$ for two rms velocities $\sigma_\mathcal{U} = 5.9$ (top line) and 10.4 cm/s (bottom line), and for three values of the wave damping prefactor by turbulence (from left to right) $C_\delta = 0$ (no damping by turbulent advection), 0.5, and 1. We observe that waves are forced by turbulence when there is an overlap between the advection region ($\omega \leq k\sigma_\mathcal{U}$) and the dispersion-relation region, that is, for large enough turbulent intensity, i.e., $\sigma_\mathcal{U}$. In this case (bottom line), and if dissipation is low, we observe concentration of signal energy on the dispersion relation. If dissipation is larger, as it is estimated in the experiment due to wave advection, less energy is transmitted to the waves on the dispersion relation, which are less energized.

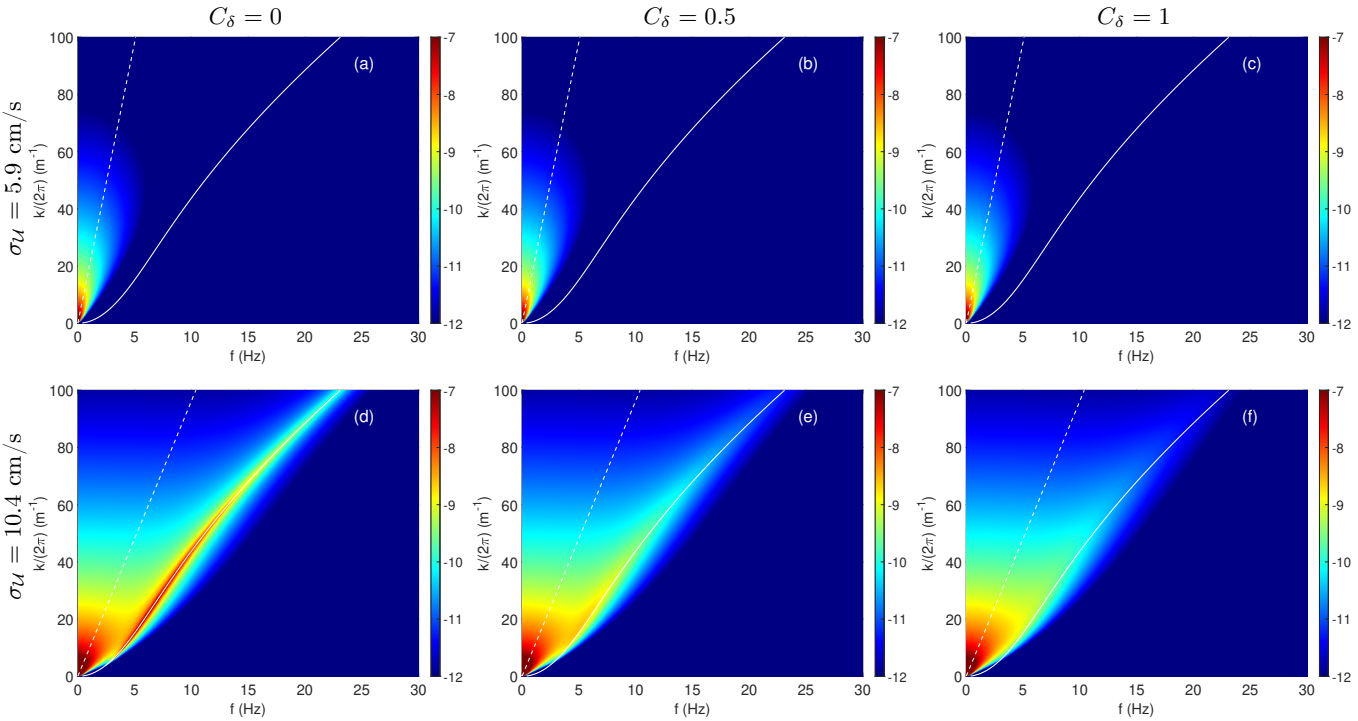


FIG. 8. Model of passive response to turbulent pressure fluctuations. Spatiotemporal spectra of surface deformations $S_\eta(k,\omega)$ for two rms velocities $\sigma_\mathcal{U} = 5.9$ (top line, a-c) and 10.4 cm/s (bottom line, d-f), and for three values of the damping prefactor $C_\delta = 0$ (no damping by turbulent advection) (a,d), 0.5 (b,e), and 1 (c,f) (from left to right).

[1] O. M. Phillips, On the generation of waves by turbulent wind, J. Fluid Mech. **2**, 417 (1957).

[2] M. A. C. Teixeira and S. E. Belcher, On the initiation of surface waves by turbulent shear flow, Dyn. Atmos. Oceans **41**, 1 (2006).

[3] M. Brocchini and D. H. Peregrine, The dynamics of strong turbulence at free surfaces. Part 1. Description, J. Fluid Mech. **449**, 225 (2001).

[4] S. Perrard, A. Lozano-Durán, M. Rabaud, M. Benzaquen, and F. Moisy, Turbulent windprint on a liquid surface, J. Fluid Mech. **873**, 1020 (2019).

[5] L. Deike, Mass transfer at the ocean–atmosphere interface: the role of wave breaking, droplets, and bubbles, Annu. Rev. Fluid Mech. **54**, 191 (2022).

[6] A. Calado and E. Balaras, Interfacial deformation and energy exchange in free-surface turbulence. J. Fluid Mech. **1025**, A52 (2025).

[7] P. A. Bullee, S. Weichert, A. Nore, D. Li, Y. Jooss, and R. J. Hearst, The influence of water turbulence on surface deformations and the gas transfer rate across an air–water interface, Exp. Fluids **65**, 132 (2024).

[8] D. Wüthrich, R. Shi, and H. Chanson, Strong free-surface turbulence in breaking bores: a physical study on the free-surface dynamics and air–water interfacial features, J. Fluid Mech. **924**, A20 (2021).

[9] F. Muraro, G. Dolcetti, A. Nichols, S. J. Tait, and K. V. Horoshenkov, Free-surface behaviour of shallow turbulent flows, J. Hydraul. Res. **59**, 1 (2021), and references therein.

[10] S. Loewen, B. Ahlborn, and A. B. Filuk, Statistics of surface flow structures on decaying grid turbulence, Phys. Fluids **29**, 2388 (1986).
[11] S. Kumar, R. Gupta, and S. Banerjee, An experimental investigation of the characteristics of free-surface turbulence in channel flow, Phys. Fluids **10**, 437 (1998).
[12] R. Savelsberg and W. van de Water, Experiments on free-surface turbulence, J. Fluid Mech. **619**, 95 (2009).
[13] T. Jamin, M. Berhanu, and E. Falcon, Experimental study of three-dimensional turbulence under a free surface, Phys. Rev. Fluids **10**, 034608 (2025).
[14] E. A. Variano and E. A. Cowen, A random-jet-stirred turbulence tank, J. Fluid Mech. **604**,1 (2008).
[15] D. J. Ruth and F. Coletti, Structure and energy transfer in homogeneous turbulence below a free surface, J. Fluid Mech. **1001**, A46 (2024).
[16] J. C. R. Hunt and J. M. R. Graham, Free-stream turbulence near plane boundaries, J. Fluid Mech. **84**, 209 (1978).
[17] M. A. C. Teixeira and S. E. Belcher, Dissipation of shear-free turbulence near boundaries, J. Fluid Mech. **422**, 167 (2000).
[18] J. Magnaudet, High-Reynolds-number turbulence in a shear-free boundary layer: revisiting the Hunt-Graham theory, J. Fluid Mech. **484**, 167 (2003).
[19] Y. Qi, Y. Li, and F. Coletti, Small-scale dynamics and structure of free-surface turbulence, J. Fluid Mech. **1005**, A8 (2025).
[20] J. R. Aarnes, O. M. Babiker, A. Xuan, L. Shen, and S. Å. Ellingsen, Vortex structures under dimples and scars in turbulent free-surface flows, J. Fluid Mech. **1007**, A38 (2025).
[21] O. M. Babiker, J. R. Aarnes, A. Semati, A. Ferran, Y. H. Tee, R. J. Hearst, and S. Å. Ellingsen, The relationship between surface features and sub-surface turbulence: simulations and experiments, arXiv:2510.03732v1 (2025).
[22] C. Guo and L. Shen, Interaction of a deformable free surface with statistically steady homogeneous turbulence, J. Fluid Mech. **658**, 33 (2010).
[23] T. Jamin, *Interactions between free-surface waves and hydrodynamic flows*, Ph.D. thesis, Univ. Paris Diderot, 2016 (in French).
[24] P. Gutiérrez and S. Aumaître, Surface waves propagating on a turbulent flow, Phys. Fluids **28**, 025107 (2016).
[25] C. Falcón and S. Fauve, Wave-vortex interaction, Phys. Rev. E **80**, 056213 (2009).
[26] B. K. Smeltzer, O. Rømcke, R. J. Hearst, and S. Å. Ellingsen, Experimental study of the mutual interactions between waves and tailored turbulence, J. Fluid Mech. **962**, R1 (2023).
[27] M. Takeda and K. Mutoh, Fourier transform profilometry for the automatic measurement of 3D object shapes, Appl. Opt. **22**, 3977 (1983).
[28] P. J. Cobelli, A. Maurel, V. Pagneux, and P. Petitjeans, Global measurement of water waves by Fourier transform profilometry, Exp. Fluids **46**, 1037 (2009).
[29] E. Falcon and E. Mordant, Experiments in surface gravity-capillary wave turbulence, Annu. Rev. Fluid Mech. **54**, 1 (2022).
[30] Industrial titanium dioxide (0.3-µm TiO_2) pigment (Anatase) from Kronos^{TM}. Product Code: 1002
[31] A. Przadka, B. Cabane, V. Pagneux, A. Maurel, and P. Petitjeans, Fourier transform profilometry for water waves: How to achieve clean water attenuation with diffusive reflection at the water surface?, Exp. Fluids 52, 519 (2012).
[32] See Supplemental Material at [URL] for a movie showing free-surface deformations as scars and waves in response to subsurface moderate turbulence (oblique view).
[33] E. Falcon and G. Ricard, Experimental quasi-1D capillary-wave turbulence, Europhys. Lett. (EPL), **135**, 64001 (2021).
[34] P. Gutiérrez, *Effects on the free surface of a turbulent flow*, Ph.D. thesis, CEA Saclay, France, 2013 (in French).
[35] V. E. Zakharov and N. N. Filonenko, Energy spectrum for stochastic oscillations of the surface of a liquid, Sov. Phys. Dokl. **11**, 881 (1967).
[36] V. E. Zakharov, V. Lvov, and G. Falkovich, *Kolmogorov-Zakharov Spectra of Turbulence* (2nd Ed., Springer, Berlin, 2025).
[37] G. F. Rota, A. Mazzino, and M. E. Rosti, Free surfaces in turbulence–a unified framework from water surfaces to elastic solids, ArXiv:2605.23166 (2026).
[38] O. M. Phillips, The equilibrium range in the spectrum of wind-generated waves, J. Fluid Mech. **4**, 426 (1958).
[39] K. W. Melville, L. Lenain, D. R. Cayan, M. Kahru, J. P. Kleissl, P. F. Linden, and N. M. Statom, The modular aerial sensing system, J. Atmos. Oceanic Technol. **33**, 1169 (2016).
[40] V. E. Zakharov and N. N. Filonenko, Weak turbulence of capillary waves, J. Appl. Mech. Tech. Phys. **8**, 37 (1967).
[41] A.S. Monin and A.M. Yaglom, *Statistical Fluid Mechanics. Vol. 2.* (MIT, Cambridge, MA, 1975).
[42] Y. Tsuji and T. Ishihara, Similarity scaling of pressure fluctuation in turbulence, Phys. Rev. E **68**, 026309 (2003).
[43] O. Terashima, Y. Sakai, and K. Nagata, Simultaneous measurement of velocity and pressure in a plane jet, Exp. Fluids **53**, 1149 (2012).
[44] O. M. Phillips, Spectral and statistical properties of the equilibrium range in wind-generated gravity waves, J. Fluid Mech. **156**, 505 (1985).
[45] T. Gotoh and D. Fukayama, Pressure Spectrum in Homogeneous Turbulence, Phys. Rev. Lett. **86**, 3775 (2001).
[46] S. Fauve, S. Laroche, and B. Castaing, Pressure fluctuations in swirling turbulent flows, J. Phys. II France **3**, 271, 1993.
[47] M. Wilczek and Y. Narita, Wave-number–frequency spectrum for turbulence from a random sweeping hypothesis with mean flow, Phys. Rev. E **86**, 066308 (2012).
[48] H. S. Ölmez and J. H. Milgram, An experimental study of attenuation of short water waves by turbulence, J. Fluid Mech. **239**, 133 (1992).
[49] H. Lamb, *Hydrodynamics* (6th Ed., Dover, New York, 1932).
[50] L. Deike, M. Berhanu, and E. Falcon, Energy flux measurement from the dissipated energy in capillary wave turbulence, Phys. Rev. E **89**, 023003 (2014), and references therein.

[51] P. Clark di Leoni, P. J. Cobelli, and P. D. Mininni, The spatio-temporal spectrum of turbulent flows, Eur. Phys. J. E **38**, 136 (2015).
[52] E. Falcon, J.-C. Bacri, and C. Laroche, Dissipated power within a turbulent flow forced homogeneously by magnetic particles, Phys. Rev. Fluids 2, 102601 (R) (2017).
[53] A. Cazaubiel, J.-B. Gorce, J.-C. Bacri, M. Berhanu, C. Laroche, and E. Falcon, Three-dimensional turbulence generated homogeneously by magnetic particles, Phys. Rev. Fluids **6**, L112601 (2021).
[54] J.-B. Gorce and E. Falcon, Statistical equilibrium of large scales in three-dimensional hydrodynamic turbulence, Phys. Rev. Lett. **129**, 054501 (2022).